

1 **Three-Dimensional S-Wave Velocity Structure of the Kinki Region,**
2 **Southwestern Japan based on Ambient Seismic Noise Tomography using Data**
3 **from Dense Seismic Array**

4 **B. Nthaba^{1,2}, T. Ikeda^{1,3}, H. Nimiya^{1,4}, T. Tsuji^{1,3*}, and Y. Iio⁵**

5 ¹ Department of Earth Resources Engineering, Kyushu University, Fukuoka, Japan,

6 ² Earth and Environmental Sciences Department, Botswana International University of Science
7 and Technology, P/Bag 16, Palapye, Botswana,

8 ³ International Institute for Carbon-Neutral Energy Research, Kyushu University, Fukuoka,
9 Japan,

10 ⁴ Geological Survey of Japan, National Institute of Advanced Industrial Science and Technology
11 (AIST), Ibaraki, Japan,

12 ⁵ Disaster Prevention Research Institute, Kyoto University, Kyoto, Japan.

13 Corresponding author: Takeshi Tsuji (tsuji@mine.kyushu-u.ac.jp)

14 **Key Points:**

- 15 • We estimated a high-resolution three-dimensional S-wave velocity model of the Kinki
16 region using ambient noise tomography
- 17 • Our velocity model reveals the NE-SW trending Niigata-Kobe Tectonic Zone and the
18 highly-active Biwako-seigan Fault System
- 19 • The unidentified probable fault zones were inferred from our fine-scale linear low-
20 velocity anomalies and distribution of earthquakes

21 **Abstract**

22 Research interest in the Kinki region, southwestern Japan, has been aroused by the frequent
23 occurrence of microearthquake activity, particularly on the northern side of the Arima-Takatsuki
24 Tectonic Line. Previous studies in this area focused mainly on deep, large-scale structures and
25 could not efficiently resolve fine-scale (~10 km) shallow crustal structures. Hence,
26 characterization of the upper crustal structure of this region at an improved spatial resolution is
27 required. By cross-correlating the vertical components of the continuous ambient seismic noise
28 data from a dense seismic array, we estimated Rayleigh wave phase velocities using a frequency
29 domain method. The 3D S-wave velocity structure of the Kinki region was then obtained by
30 applying a direct surface wave tomographic method for the phase velocity dispersion data. The
31 estimated velocity model reveals a NE-SW trending low-velocity structure coinciding with the
32 Niigata-Kobe Tectonic Zone (NKTZ) and the active Biwako-seigan Fault Zone (BSFZ). Also,
33 we identified fine-scale low-velocity structures coinciding with known active faults on the
34 eastern side of the NKTZ, as well as sets of low-velocity structures across the Tanba region, that
35 may be attributable to the weathering effects or activity of unidentified concealed fault zones.
36 Furthermore, sedimentary basins manifest as low-velocity zones extending to depths ranging
37 from ~1.5 to 2 km, correlating with those reported in previous studies. Our results therefore
38 contribute towards fundamental understanding of earthquake faulting as well as tectonic
39 boundary and will be useful for hazard assessment and disaster mitigation.

40 **Plain Language Summary**

41 Due to the frequent occurrence of low-intensity earthquakes in the Kinki region, southwestern
42 Japan, there has been a keen research interest aimed at understanding the Earth's internal
43 structure in this region. Geophysical methods based on the speed of seismic waves have been
44 employed by other researchers to examine the structural make-up of the Earth's interior in a wide
45 area. In the Kinki region, previous studies focused on deep, large-scale features of the earth and
46 could not sufficiently map shallow, small-sized (~10 km) structures. In this study, we used
47 ambient vibrations of the earth to extract seismic wave speeds information. Then, we constructed
48 a high-resolution three-dimensional geological model based on seismic wave speeds using
49 specialized geophysical method. Our results reveal linear low-speed zones, interpreted as
50 documented active fault zones and undocumented probable fault zones. These features could be
51 linked to the frequent occurrence of earthquakes in the Kinki region. Our results contribute
52 towards improved understanding of the shallow crustal structure in the Kinki region and can be
53 used to identify earthquake-prone zones, thus facilitating disaster risk reduction. Furthermore, we
54 can use the information of seismic wave speed for accurate earthquake hypocenter estimation.

55 **1 Introduction**

56 To unravel heterogeneities within the crustal structure and upper mantle over a wide area, very
57 few geophysical techniques with proven efficacy are available (Suemoto et al., 2020). Ground-
58 based geophysical methods such as active-source seismic reflection and refraction techniques can
59 be used to map the distribution of faults and geologic boundaries at high resolution. A striking
60 example is a study by Sato et al. (2009), in which deep seismic reflection profiling was employed
61 along a 135 km long seismic line from Metropolitan Osaka to the Ise basin (Osaka-Suzuka seismic
62 survey) across several active reverse faults. Likewise, Ito et al. (2006) conducted a similar survey
63 along the N-S-trending Shingu-Maizuru line. However, this approach only provides details about
64 fault locations and geologic boundaries along the profiles, and heterogeneities across the profiles

65 can only be established from multiple profiles. Therefore, this approach is not well suited to
66 constructing large-scale geological models for areas as large as the Kinki region.

67 Conversely, P- and S-wave travel-time tomography using local earthquake data over a wide area
68 has provided significant results, resolving major structures such as faults and geologic boundaries
69 (Matsubara et al., 2008; Nakajima et al., 2009; Yolsal-Cevikbilen et al., 2012). Even so, the
70 downside of this approach is that the resolution of geological structures depends on the distribution
71 of natural earthquakes (Suemoto et al., 2020). Using teleseismic data, surface wave tomography
72 can also be applied but teleseismic propagation paths complicate short period (<20 s)
73 measurements due to the scattering and attenuation that occur as distant waves propagate (Bensen
74 et al., 2007; Yang, 2014). Such short-period measurements are the core of our objectives in this
75 study as we seek to resolve shallow crustal features within the Kinki region.

76 The emergence of ambient noise tomography (ANT) in the last decade has revolutionized seismic
77 tomography because it can circumvent the shortcomings of traditional earthquake surface wave
78 tomography (Sabra et al., 2005; Shapiro et al., 2005). This method utilizes diffuse background
79 ground motion (ambient noise) to extract surface wave empirical Green's functions between
80 station pairs by cross-correlating continuously recorded seismic waveforms (Yang, 2014). It is
81 therefore convenient because surface wave dispersion curves between station pairs can be
82 estimated without requiring the occurrence of earthquakes, as each station can serve as a virtual
83 source and a receiver (Yang, 2014). Since the inception and further developments of permanent
84 and temporary high-quality seismic networks, ANT has been applied to estimate subsurface
85 structures in various geological settings (Chen et al., 2018; Lin et al., 2008; Nishida et al., 2008;
86 Shapiro et al., 2005). Suemoto et al. (2020) constructed a high-resolution shallow-crustal S-wave
87 velocity structure by ambient noise surface wave tomography in the San-in area using data
88 recorded by several seismic arrays, comprising Hi-net stations (Obara et al., 2005) and the dense
89 Manten project array (Iio et al., 2018). Similarly, Nimiya et al. (2020) successfully utilized surface
90 wave data extracted from ambient noise recorded by Hi-net stations to estimate the 3D S-wave
91 velocity structure of central Japan. In contrast, there is still no detailed information about the 3D
92 S-wave velocity structure of the Kinki region.

93 To provide an improved constraint on fine-scale (~10 km) shallow-crustal structures and
94 geological boundaries in the Kinki region, we performed ambient noise tomographic inversion.
95 We constructed a high-resolution shallow S-wave velocity model using data recorded by the
96 widely distributed Hi-net stations and Japan Meteorological Agency (JMA) stations integrated
97 with data recorded by densely distributed Manten project seismic stations (Iio et al., 2018; Katoh
98 et al., 2019). From our model, the geometry and spatial distribution of major faults and geological
99 boundaries are estimated.

100 **2 Geologic setting**

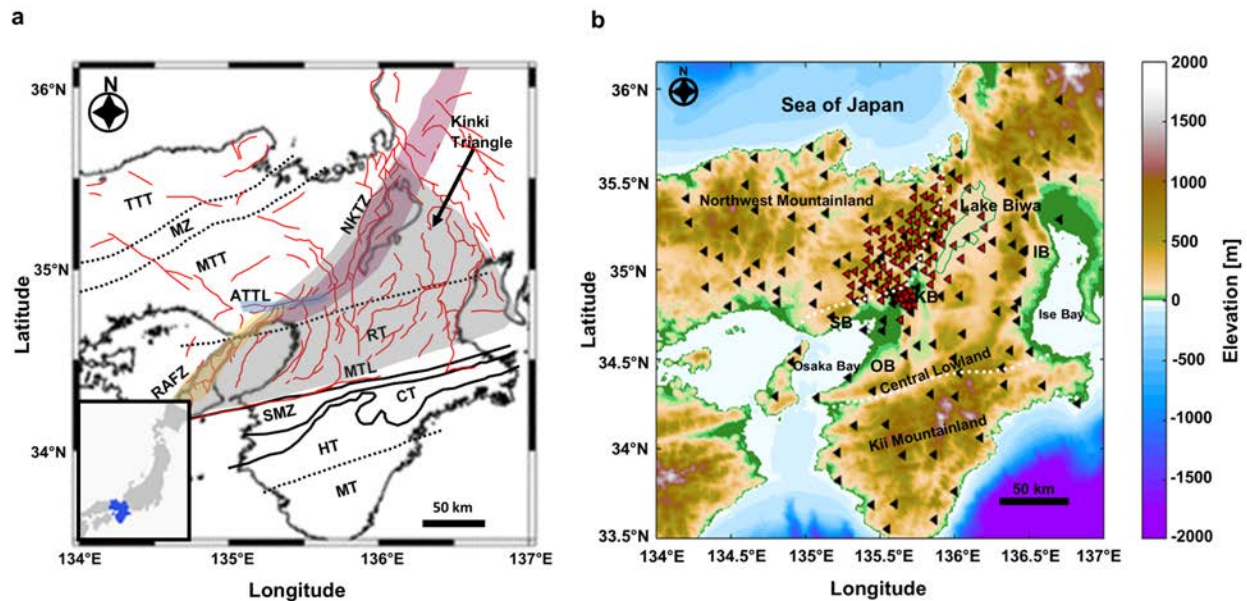
101 In the Kinki region, southwestern Japan, the Philippine Sea (PHS) oceanic plate subducts beneath
102 the overriding Eurasian (EUR) plate (Aoki et al., 2016). The southeastward movement of the
103 incipient Amurian plate (Amur Plate) with respect to the EUR plate and a shift in the direction of
104 subduction of the PHS plate (Taira, 2001) has generated relatively new, large fault zones or
105 continually reactivates the old ones, a process referred to as neotectonics (Barnes, 2008).

106 The major contributors in neotectonics faulting in the Kinki region comprise, among others, the
107 Median Tectonic Line (MTL; black line in Figure 1a), which has been reactivated but now in the
108 right-lateral direction, opposing the Cretaceous left-lateral strike-slip fault action (Barnes, 2008).
109 The MTL divides the Kinki region into outer zone and inner zone (Matsushita, 1963). On the one
110 hand, the outer zone is characterized by four zonally arranged terrains from north to south: namely,
111 the Sanbagawa metamorphic terrain, Chichibu terrain, Hidaka terrain, and Muro terrain (SMZ, CT,
112 HT, and MT; Figure 1a). On the other hand, the zonal arrangement of geologic formations in the
113 inner zone is not prominent, it is divided from north to south into the Tango–Tajima terrain
114 (composed largely of Neogene volcanic and sedimentary series), the Maizuru zone (consisting of
115 Permian and Triassic marine formations and Yakuno intrusive rocks), the Mino–Tanba terrain
116 (including Cretaceous granite), and the Ryoike terrain consisting primarily of Ryoike metamorphic
117 rocks and granites (TTT, MZ, MTT, and RT; Figure 1a) (Matsushita, 1963).

118 Huzita (1980) reported a triangular neotectonics province (the Kinki triangle, gray-shaded area in
119 Figure 1a) with the E–W compressional stress state and the alternating basins and mountain
120 topography from east to west, which provided central Japan with its civilizational homelands,
121 including the Nara, Osaka, Kyoto and Ise basins (Barnes, 2008). The Kinki triangle is
122 characterized by a dense distribution of predominantly NS-trending Quaternary active faults and
123 some NE-SW or NW-SE strike-slip active faults (Research Group for Active Faults of Japan,
124 1991). The predominantly E–W compressional movement in the upper crust has engendered the
125 uplifted mountains between the Osaka and Ise basins as a pop-up structure (Sato et al., 2009). A
126 plethora of historical large and destructive earthquakes have occurred in the Kinki region and
127 surrounding areas (Hyodo & Hirahara, 2003; Usami, 2003), mainly in the Jurassic Tanba
128 Accretionary Complex (Wakita, 2013), sharply bounded by the ENE-WSW dextral strike-slip
129 Arima-Takatsuki Tectonic Line (ATTL) to the south (Hallo et al., 2019; Iio, 1996; Katao et al.,
130 1997; Matsushita & Imanishi, 2015) and the reactivated Niigata-Kobe Tectonic Zone (NKTZ) to
131 the east, which is characterized by high strain rates (Sagiya et al., 2000). In recent times, low
132 magnitude earthquakes have been recorded across the entire Tanba region, but their locations do
133 not always coincide with known faults (Kato & Ueda, 2019). However, in such cases, the
134 distribution of their hypocenters makes a chain of seismic alignment between pairs of faults (Oike,
135 1976). This alignment suggests the possible existence of concealed active faults in those areas, or
136 continuity of known fault systems. Therefore, the possible existence of concealed faults in those
137 areas needs to be investigated in high resolution.

138 Around the Osaka area, numerous active faults exist, including the E-W to NE-SW oriented dextral
139 strike-slip faults and the N-S striking reverse faults (Research Group for Active Faults of Japan,
140 1991). The significance of these faults was highlighted by the highly catastrophic 1995 M_w 7.2
141 Kobe earthquake, which resulted from dextral strike-slip displacements on the NE–SW striking
142 Rokko-Active Fault Zone (Kanamori, 1995; Katao et al., 1997). In addition, a shallow crustal
143 earthquake of magnitude M_w 5.6 occurred in 2018, proximal to the junction of the eastern part of
144 the ATTL and the east-dipping reverse active fault systems, the Uemachi and Ikoma fault zones
145 (Kato & Ueda, 2019; Sato et al., 2009). These earthquakes are a testament to how susceptible life
146 is to tectonic movement along these fault lines and highlight the need to identify zones prone to
147 strong crustal movement in a quest to minimize the effects of destructive earthquakes. Such zones
148 include concealed fault zones, which are difficult to ascertain from surficial evidence, as well as
149 active and new fault systems, which are likely to be the locus of future events.

150



151

Figure 1. (a) Map of the Kinki region showing the spatial distribution of tectonic structures. Red lines represent active faults (retrieved on 19 November 2021 from <https://gbank.gsj.jp/subsurface/english/ondemand.php>), thick purple, yellow, and light blue lines represent the Niigata-Kobe Tectonic Zone (NKTZ), Rokko Active Fault Zone (RAFZ), and the Arima-Takatsuki Tectonic Line (ATTL), respectively. Also shown are the locations of the Median Tectonic Line (MTL), and tectonic divisions of the Kinki region, comprising Tango-Tajima Terrain (TTT), Maizuru Zone (MZ), Mino-Tamba Terrain (MTT), Ryoko Terrain (RT), Sanbagawa Metamorphic Zone (SMZ), Chichibu Terrain (CT), Hidaka Terrain (HT), and Muro Terrain (MT). The insert shows the location of the Kinki region within Japan. (b) Topographic map of the Kinki region. Red and black triangles represent the locations of temporary and permanent stations, respectively. White, broken lines indicate the boundaries between the Northwestern Mountainland, Central Lowland, and Kii Mountainland.

163

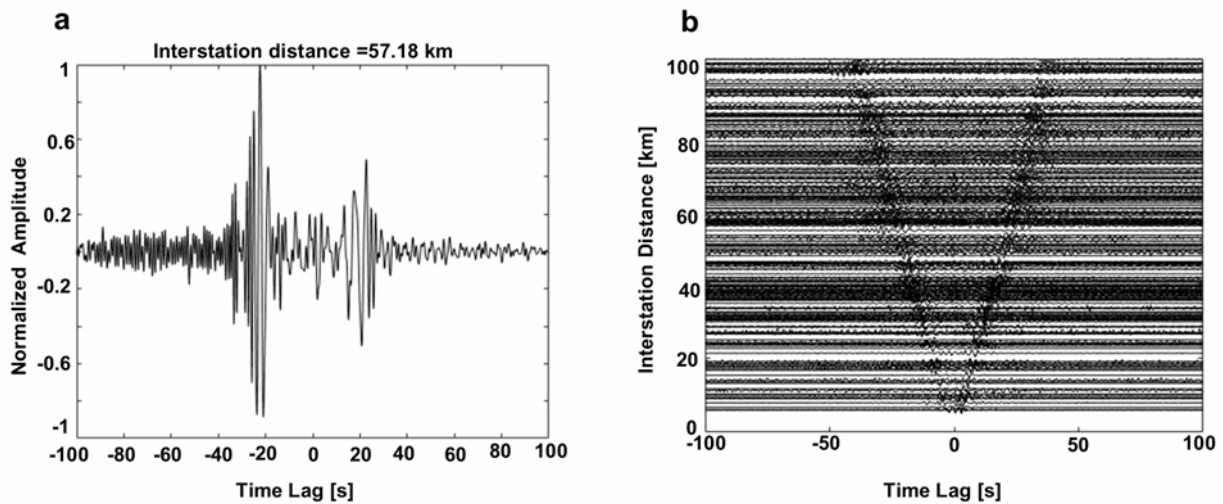
164 3 Data and Methods

165 We used the vertical component of continuous seismic waveforms recorded by permanent and
 166 temporary stations from April 1 to September 30 during the year 2019. The permanent stations
 167 included 78 Hi-net stations, 1 Kyushu University station, 1 Tokyo University station, 2 Nagoya
 168 University stations, 10 AIST stations, 16 Kyoto University stations and 9 JMA stations, and
 169 temporary stations comprised 104 Kyoto University Manten project stations (Iio et al., 2018; Katoh
 170 et al., 2019), that are distributed around the central part of the Kinki region. Combining these set
 171 of stations enabled us to obtain a dataset with very dense ray paths coverage of short-period surface
 172 waves and a subsequent high-resolution 3D S-wave velocity structure. To construct the 3D S-wave
 173 velocity structure, we first extracted surface waves propagating between station pairs by
 174 computing the cross-correlation of ambient noise. We then employed the zero-crossing method
 175 (Ekström et al., 2009) to estimate Rayleigh wave phase velocities between station pairs. Finally,
 176 we used the direct surface wave inversion (Fang et al., 2015) to obtain the 3D S-wave velocity
 177 model.

178

179 **3.1 Preprocessing and cross-correlation**

180 After partitioning continuous ambient noise data for each day into 30 minute segments with a 50%
 181 overlap, the instrumental response of each dataset was corrected. Next, cross-correlation spectra
 182 for all possible combinations of station pairs were computed from the resulting seismograms
 183 (Ekström, 2014). Then, the daily cross-correlation spectra were stacked over a six-month-long
 184 time series. Rayleigh wave propagation can be clearly observed in the time-domain cross-
 185 correlation computed from the stacked cross-correlation spectra (Figure 2).



186

187 **Figure 2.** Cross-correlation functions of the vertical component in the 0.05-0.95 Hz frequency band
 188 showing the empirical Green's functions between station pairs. (a) Cross-correlation function for a station
 189 pair with an interstation distance of 57.18 km (shown in Figure 3b), and (b) stacked cross-correlation
 190 functions from randomly selected station pairs, exhibiting surface wave propagation between station
 191 pairs.

192

193 **3.2 Surface wave phase velocity measurement**

194 Phase velocity measurements can be performed in either the frequency domain or time domain. In
 195 the time domain, only those interstation distances exceeding three wavelengths (λ) are typically
 196 considered due to the high-frequency approximation required in time domain analysis (Bensen et
 197 al., 2007; Lin et al., 2008; Yao et al., 2006). In contrast, there is no theoretical limitation for
 198 interstation distances in the frequency domain method (i.e., zero-crossing method; Ekström et al.,
 199 2009), and interstation distances up to approximately one wavelength can be practically used
 200 (Ekström et al., 2009; Tsai & Moschetti, 2010). We applied the zero-crossing method to estimate
 201 phase velocities between station pairs. The zero-crossing method is based on modeling cross-
 202 correlation spectra by the spatial autocorrelation (SPAC) method (Aki, 1957; Asten, 2006) and
 203 uses the zero-crossing frequencies of the real part of the cross-correlation spectra. The SPAC
 204 method is premised on the assumption that ambient noise is dominated by surface waves and that
 205 ambient noise sources are distributed uniformly (Aki, 1957). Under this assumption, the real part

206 of the vertical cross-correlation spectra can be modeled using a Bessel function of the first kind
207 and zeroth order as follows:

$$208 \quad \text{Real}(\rho(f, x)) = J_0\left(\frac{2\pi fx}{C_R(f)}\right), \quad (1)$$

209 where ρ is the vertical cross-spectrum, x is the interstation distance, J_0 is the Bessel function of the
210 first kind and zeroth order, and $C_R(f)$ is the Rayleigh wave phase velocity. In the zero-crossing
211 method, we focus only on the zero crossings where both sides of equation (1) should be zero. The
212 zero-crossing points are insensitive to fluctuations in the spectral power of the background noise
213 and non-linear filtering in the data processing (Ekström et al., 2009). Using zero crossings
214 simplifies phase velocity measurements and stabilizes the estimation of phase velocities because
215 phase velocity estimation is not affected by incoherent noise (Cho et al., 2021).

216 If f_n represents the frequency of the n th observed zero crossing of the cross-correlation spectrum,
217 and Z_n denotes the n th zero of the Bessel function, we can match each f_n with the zero crossings of
218 the Bessel function to have all the possible phase velocity dispersion curves according to the
219 following equation:

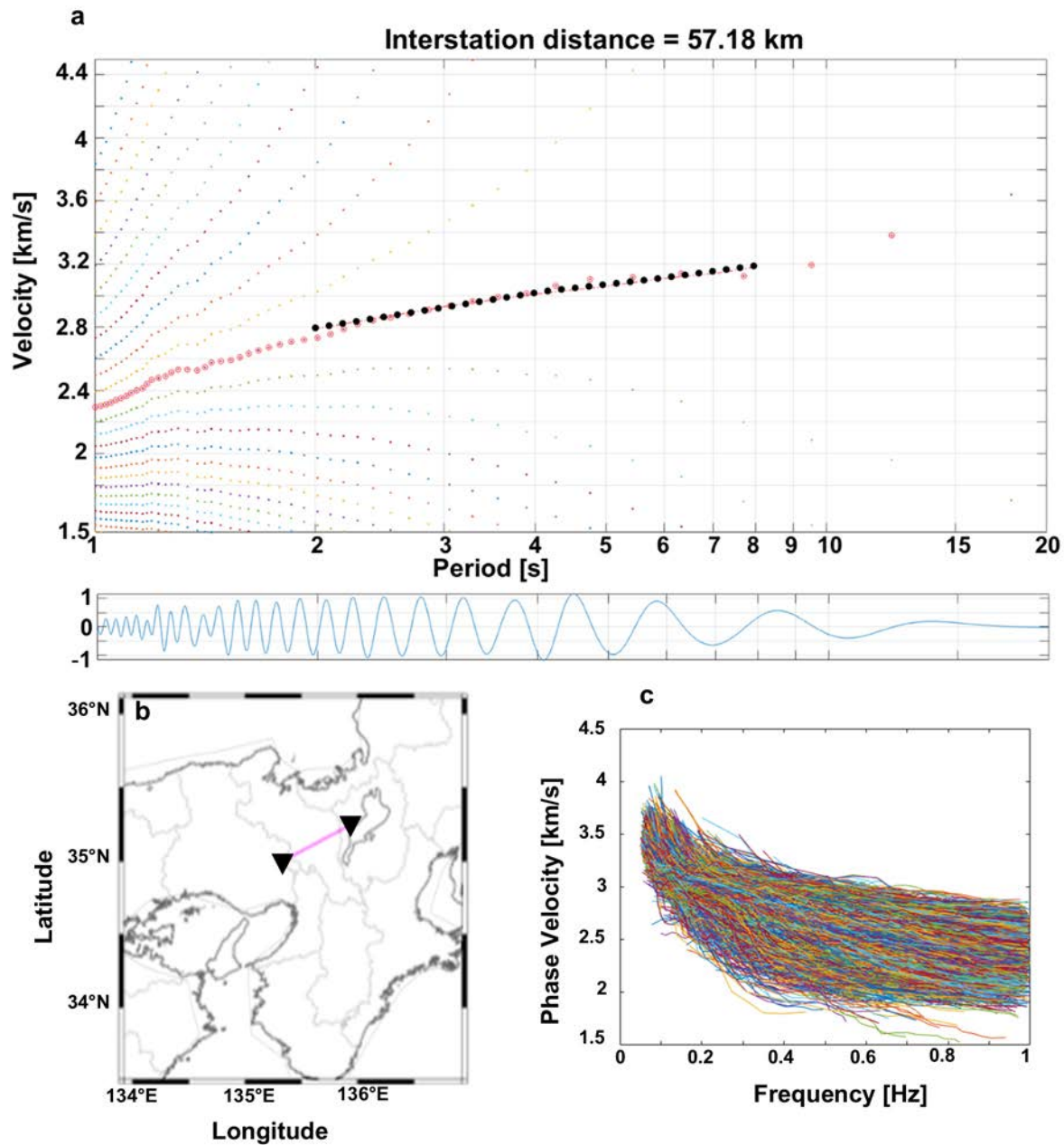
$$220 \quad C_m(f_n) = \frac{2\pi f_n x}{Z_{n+2m}}, \quad (2)$$

221 where m representing the number of missed or extra zero points, takes the values $(0, \pm 1, \pm 2, \dots)$.
222 Applying equation (2) for all observed values of f_n yields numerous possible dispersion curves.

223 We used the GSpecDisp package (Sadeghisorkhani et al., 2018) to determine Rayleigh-wave
224 phase-velocity dispersion curves uniquely by the zero-crossing method from the stacked cross-
225 correlations. To reduce noise effects in the correlations, we applied a velocity filter of 1–4.5 km/s
226 with a taper interval of ~ 0.2 km/s. Then, we applied spectral whitening to each correlation for
227 amplitude equalization (Sadeghisorkhani et al., 2018). With many possible phase velocities
228 occurring at each frequency with regard to equation (2) (colored dots; Figure 3a), it is difficult to
229 uniquely determine the phase velocity dispersion curves without using a reference velocity
230 dispersion curve as a guide. To circumvent this, we manually picked the dispersion curve
231 appearing closest to the reference dispersion curve. In the GSpecDisp, average velocities can be
232 estimated by combining all cross-correlation spectra (average velocity module). We estimated
233 average velocities in the period range from 2 to 8 s and used the result as a reference velocity for
234 dispersion curve estimation in single station-pair phase-velocity picking mode in GSpecDisp
235 (dashed black dots; Figure 3a). Finally, we estimated phase-velocity dispersion curves between
236 each station pair (red circles in Figure 3a).

237 For our dataset, the maximum measurable period required an interstation distance (x , in km) of at
238 least three wavelengths (λ), defined as the x/λ ratio in GSpecDisp ($x/\lambda \geq 3$). For each cross-
239 correlation function, the signal-to-noise ratio (SNR) was defined as the ratio between maximum
240 absolute amplitude in the signal window (between arrival times corresponding to waves with 1
241 and 4.5 km/s) and the root mean square amplitude in the noise time window (between 500 and 700
242 s). We used an SNR threshold of 10 to reject correlations with low signal. Finally, we obtained a
243 total of 23,647 dispersion curves (Figure 3c).

244



245

246 **Figure 3.** (a) Observed phase velocity dispersion curves (upper panel) and the real part of the cross-
 247 correlation spectrum (lower panel). Red and black circles in the upper panel represent the selected points
 248 of the dispersion curve and the average phase-velocity dispersion curve for the region, respectively. (b)
 249 Location of the station pair for which dispersion data are displayed in (a). (c) Phase-velocity–frequency
 250 plot showing the 23,647 selected dispersion curves for all the station pairs used.

251

252 3.3 Direct inversion of the surface wave dispersion curves

253 Ambient noise tomography using phase velocity dispersion curves typically involves a two-step
 254 procedure. Firstly, 2D phase velocity maps are constructed by travel-time tomography at discrete
 255 frequencies. Secondly, pointwise inversion of dispersion data for 1D profiles of S-wave velocity
 256 as a function of depth at each grid point is implemented, and combining multiple 1D profiles
 257 subsequently yields the 3D S-wave velocity structure (Shapiro & Ritzwoller, 2002; Yao et al.,
 258 2008). Nonetheless, a 3D S-wave velocity structure can equally be estimated by direct inversion
 259 of dispersion data without the intermediate step of constructing 2D phase velocity maps (Boschi
 260 & Ekström, 2002; Fang et al., 2015; Feng & An, 2010; Pilz et al., 2012). Typically, these direct
 261 inversion approaches do not update the ray paths and sensitivity kernels for the newly constructed
 262 3D models (Fang et al., 2015). Also, one-step linearization may produce biased wave velocity
 263 estimations in a medium akin to the shallow crustal structure, where S-wave velocity variations
 264 can exceed 20% (Lin et al., 2013).

265 To estimate the 3D S-wave velocity structure from phase velocity dispersion data, we applied a
 266 direct surface wave tomography method (DSurfTomo), which is based on frequency-dependent
 267 ray-tracing and a wavelet-based sparsity-constrained inversion (Fang et al., 2015). This approach
 268 circumvents the intermediate step of constructing 2D phase velocity maps and iteratively updates
 269 the sensitivity kernels of period-dependent dispersion data (Fang et al., 2015). Furthermore, it
 270 accounts for the ray-bending effects of period-dependent ray paths by using the fast-marching
 271 method (Rawlinson & Sambridge, 2004). Accounting for such effects in the inversion is especially
 272 useful for short-period surface waves, which are significantly sensitive to the highly complex
 273 shallow crustal structure (Fang et al., 2015; Gu et al., 2019). Therefore, this approach is a well-
 274 suited tool for determining the shallow-crustal structure of the Kinki region using short-period
 275 surface-waves dispersion data.

276 In tomographic inversion, the objective is to find a model \mathbf{m} that minimizes the differences $\delta t_i(f)$
 277 between the measured travel times $t_i^{obs}(f)$ and the calculated travel times $t_i(f)$ from the model
 278 for all frequencies f . The travel time for path i is given as

$$279 \quad \delta t_i(f) = t_i^{obs}(f) - t_i(f) \approx - \sum_{k=1}^K v_{ik} \frac{\delta C_k(f)}{C_k^2(f)}, \quad (3)$$

280 where $t_i(f)$ represents the computed travel times from a reference model that can be updated in
 281 the inversion, v_{ik} denotes the bilinear interpolation coefficients along the ray path associated with
 282 the i th travel-time data, $C_k(f)$ is the phase velocity, and $\delta C_k(f)$ denotes its perturbation at the k th
 283 2D surface grid node at frequency f . Surface wave dispersion is sensitive primarily to S-wave
 284 velocity (Fang et al., 2015). However, short-period Rayleigh wave dispersion also has a sensitivity
 285 to P-wave velocity in the shallow crust (Fang et al., 2015). The P-wave velocity perturbations
 286 together with mass density are therefore explicitly included in the calculation of surface wave
 287 dispersion, with R'_α and R'_ρ as scaling factors, leading to the following equation:

$$288 \quad \delta t_i(f) = \sum_{k=1}^K \left(-\frac{v_{ik}}{C_k^2} \right) \sum_{j=1}^J \left[R'_\alpha(z_j) \frac{\partial C_k}{\partial \alpha_k(z_j)} + R'_\rho(z_j) \frac{\partial C_k}{\partial \rho_k(z_j)} + \frac{\partial C_k}{\partial \beta_k(z_j)} \right] \Bigg|_{\theta_k} \delta \beta_k(z_j) =$$

$$289 \quad \sum_{l=1}^M G_{il} m_l, \quad (4)$$

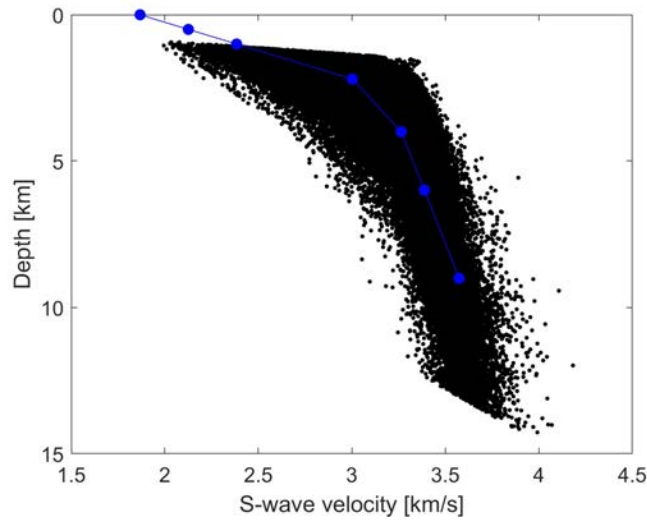
290

291 where θ_k denotes the 1D reference model at the k^{th} surface grid point, $\alpha_k(z_j)$, $\rho_k(z_j)$, and $\beta_k(z_j)$
 292 represent the P-wave velocity, the mass density, and the S-wave velocity, respectively. J is the
 293 number of grid nodes in the depth direction, and $M = KJ$ represents the total number of grid points.
 294 Equation (4) can be written in matrix form, as follows:

$$295 \quad \mathbf{d} = \mathbf{G}\mathbf{m}, \quad (5)$$

296 where \mathbf{d} is the surface wave travel-time residual vector for all ray paths and discrete frequencies,
 297 \mathbf{G} represents the data sensitivity matrix, and \mathbf{m} represents the model parameter vector. Damping
 298 and weighting parameters are applied to balance data fitting and smoothing regularization. In
 299 addition to the damping and weighting parameters, the sparsity fraction, which is a parameter
 300 indicating how sparse the sensitivity matrix is, was selected on a trial-and-error basis for our data
 301 considering the diverse patterns in inverted S-wave velocity models (weakly smoothed and
 302 strongly smoothed S-wave velocity models are shown in Figures S1 and S2, respectively).

303 In our inversion, the entire Kinki region was parameterized into 55 by 60 grid points on the
 304 horizontal plane with an interval of 0.05° in each horizontal direction (latitude and longitude), as
 305 well as 7 grid points along the depth direction (i.e., 0, 0.5, 1.0, 2.2, 4.0, 6.0 and 9.0 km). These
 306 parameters along with the large volume of dispersion data were memory intensive, we therefore
 307 used dispersion data within a narrow frequency bandwidth of 0.083 - 0.67 Hz to circumvent the
 308 computer memory limitations during the inversion. Dispersion measurements within a broad
 309 frequency bandwidth of 0.05 - 0.95 Hz was used for the northern part of the Kinki area, which was
 310 parameterized into 29 by 96 grid points on the horizontal plane with an interval of 0.02° in the
 311 latitude and longitude directions, and 11 grid points along the vertical direction (0, 0.1, 0.3, 0.5,
 312 0.8, 1.4, 2.0, 3.0, 4.0, 5.5 and 7.0 km). Empirically, the fundamental mode Rayleigh wave phase
 313 velocity is primarily sensitive to $1.1 \times$ S-wave velocity at depths of about one-third of its
 314 corresponding wavelength (Fang et al., 2015; Foti et al., 2014; Hayashi, 2008). Consequently, an
 315 initial S-wave velocity model was constructed by multiplying the average of the observed Rayleigh
 316 wave phase velocities at a depth of one-third of the wavelength by 1.1 (i.e., a one-third wavelength
 317 transformation; Figure 4). Topographic effects on our inverted S-wave velocity models were
 318 accounted for by subtracting altitude from the depth value at each grid point because the inversion
 319 is based on the assumption of a flat surface. Therefore, the depth shown in our final 3D S-wave
 320 velocity models is the depth below sea level (S-wave velocity models before topographic
 321 correction are shown in Figures S3, S4 and S5).



322

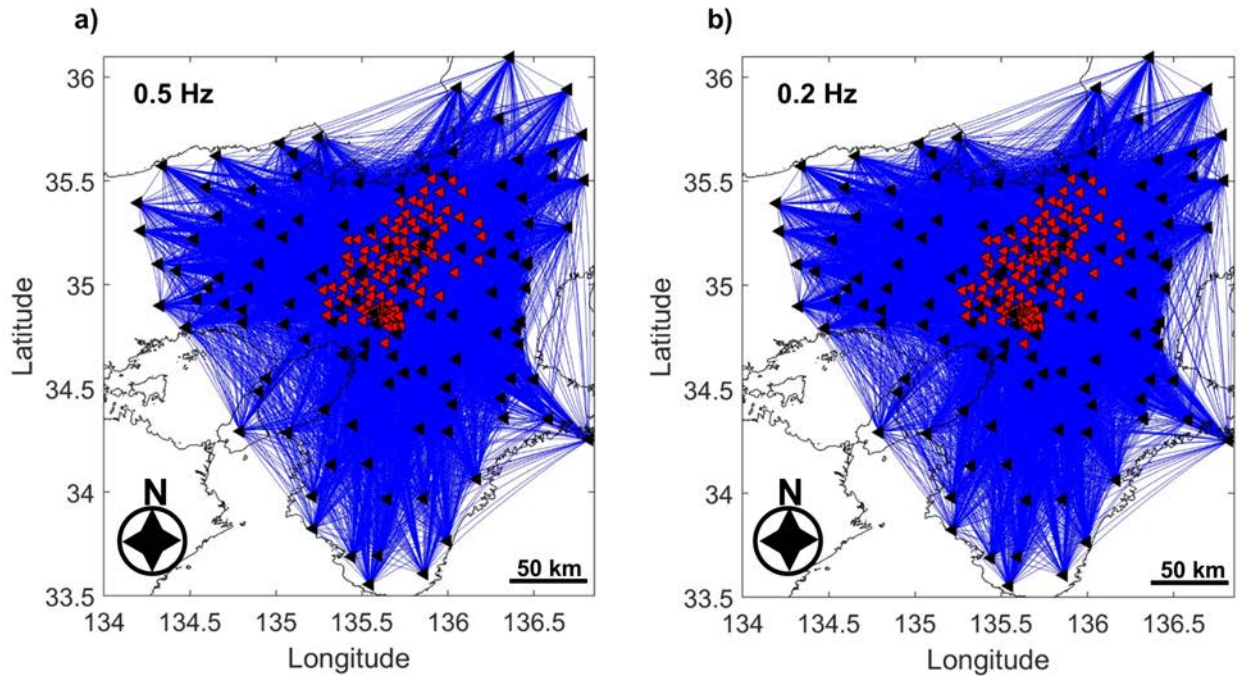
323 **Figure 4.** Initial S-wave velocity model. Black dots represent transformed interstation Rayleigh wave
 324 phase-velocity dispersion curves measured using the zero-crossing method to a depth–S-wave velocity
 325 approximation. The blue line and blue dots represent the average S-wave velocity model used as the
 326 initial reference S-wave velocity model in the inversion process.

327

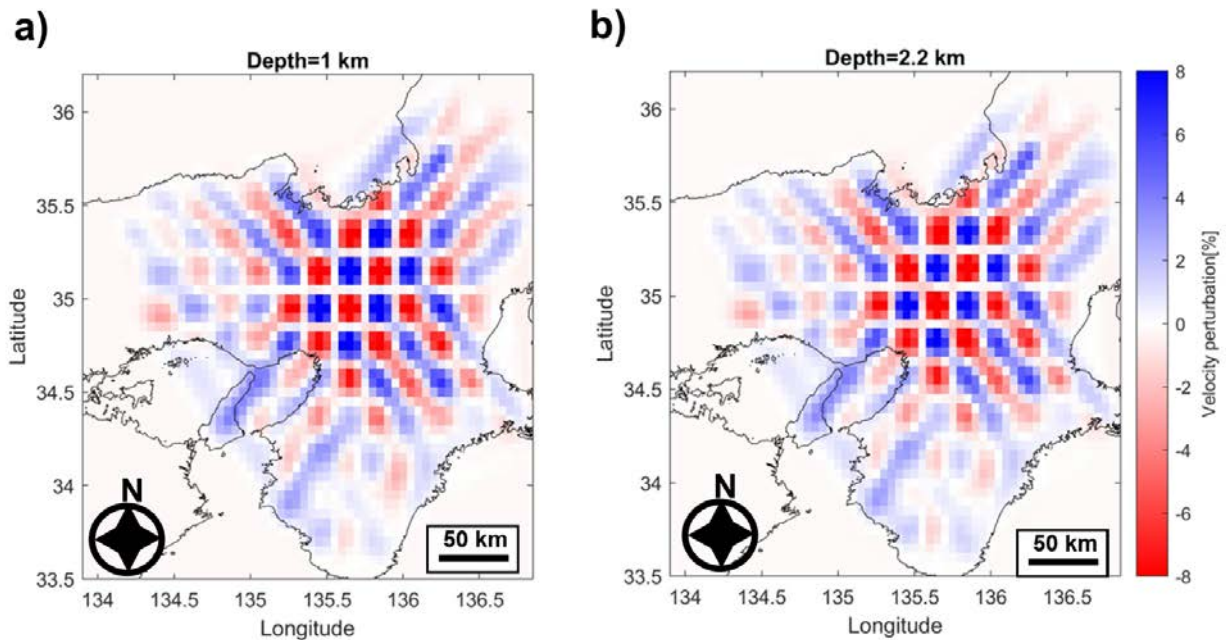
328 **4 Results**

329 We employed the direct surface wave tomographic inversion method to construct a 3D S-wave
 330 velocity model of the Kinki region using Rayleigh wave dispersion curves. To ensure the reliability
 331 of our measurements, we plotted the spatial ray paths coverage within the Kinki region (Figure 5).
 332 From Figure 5, it is apparent that the ray paths density is sufficient to provide reliable
 333 measurements, especially in the most central part of the study area, where seismic stations are
 334 densely distributed. At the edges, however, the ray paths coverage is slightly limited. To further
 335 corroborate our inverted S-wave velocity model, we conducted a checkerboard resolution test
 336 using anomalies of $\sim 0.2^\circ$ (~ 22 km; Figure 6a, b) and $\sim 0.1^\circ$ (~ 11 km; Figure S6) for the entire Kinki
 337 region and the northern part of the Kinki region, respectively, with an amplitude of the velocity
 338 anomaly set to $\sim 10\%$. In Figure 6, we display the results of the checkerboard resolution test for
 339 horizontal slices at different depths. Using these parameters, tectonic and geologic features with
 340 sizes greater than 10 km could be resolved clearly in the center of the study area using observed
 341 data.

342



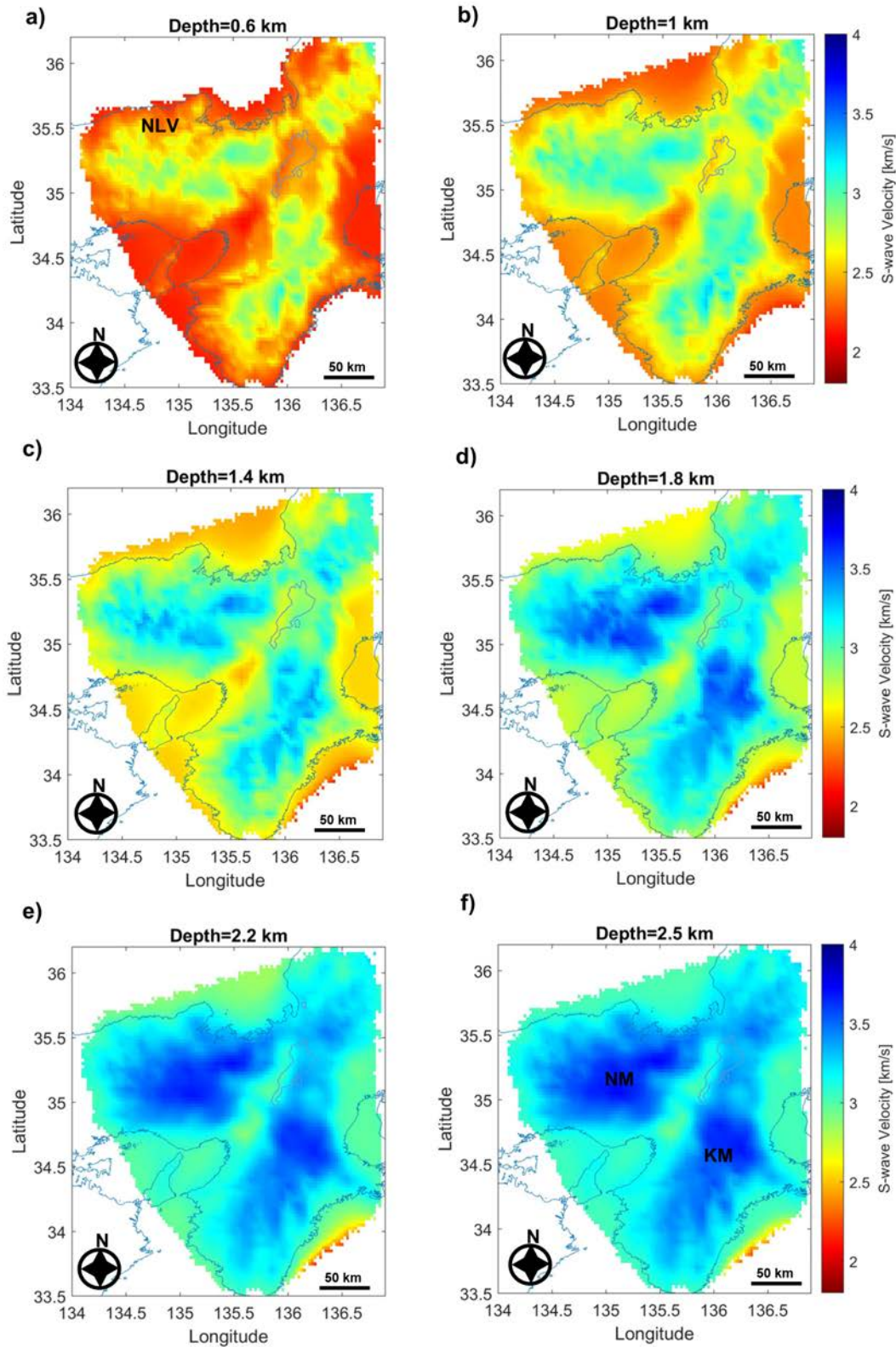
343
 344 **Figure 5.** Ray paths obtained from the final 3D inversion model at two selected frequencies by the fast-
 345 marching method: (a) 0.5 Hz and (b) 0.2 Hz. Red and black triangles represent the locations of temporary
 346 and permanent stations, respectively. Blue lines indicate ray paths.
 347



348
 349 **Figure 6.** Horizontal velocity perturbation slices of the checkerboard resolution test results at 1 km (a)
 350 and 2.2 km (b) depths. The anomaly size was ~ 22 km (0.2°), and the velocity amplitude was $\sim 10\%$. Depth
 351 is shown above each horizontal slice.
 352

353 Figure 7 displays selected horizontal slices (map views) at different depths, exhibiting the lateral
354 distribution of S-wave velocities within the study area. The third dimension (depth, in km) is given
355 in the numerical form above each horizontal slice. Significant S-wave velocity heterogeneities are
356 apparent and are discussed in detail in the following sections. These anomalies highlight tectonic
357 and geologic features associated with the study area.

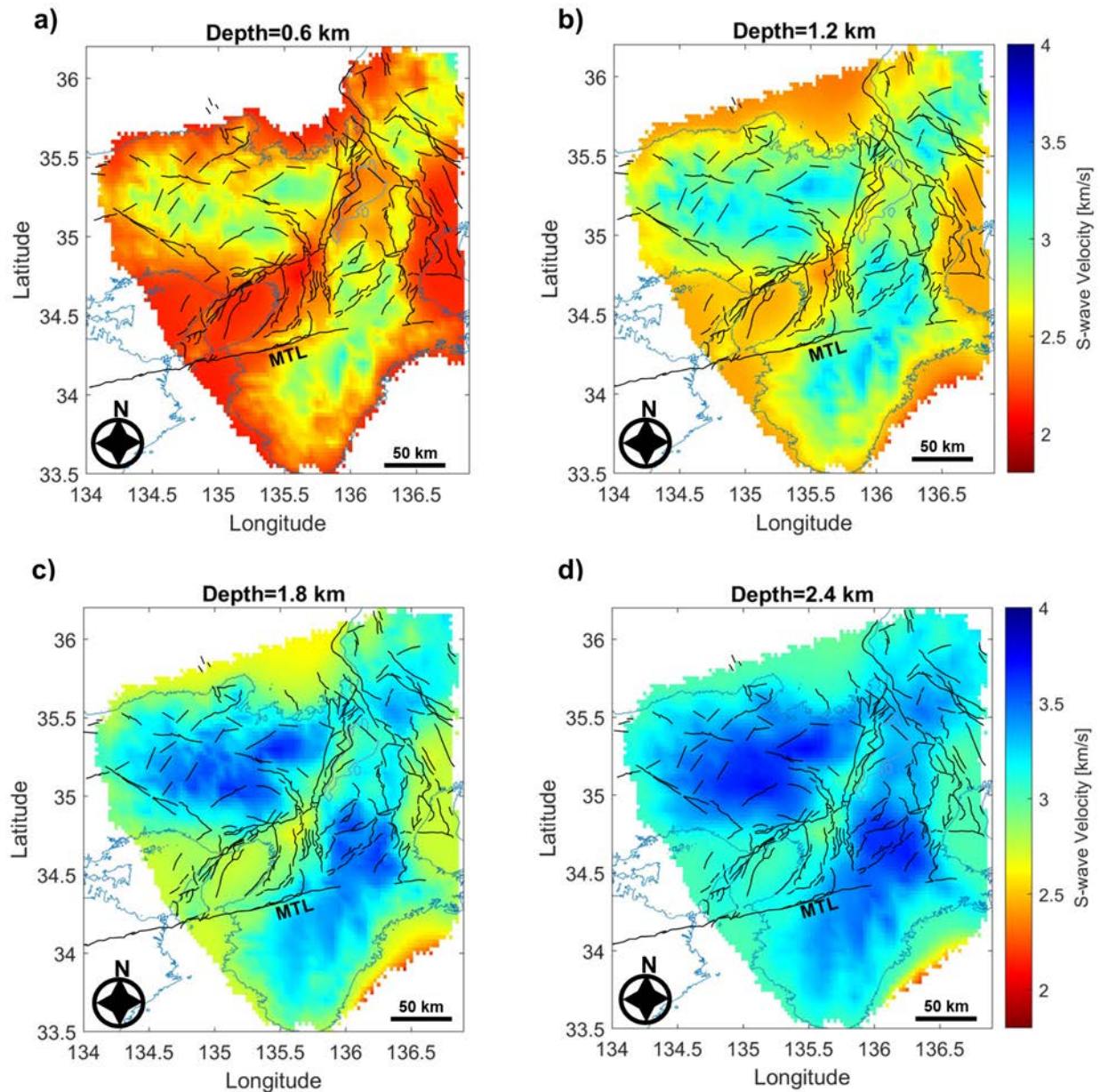
358 Two broad high-velocity anomalies can be observed in the displayed horizontal slices. The first
359 anomaly (marked NM, Figure 7f) appears to be trending in the E–W direction, whereas the second
360 high-velocity anomaly (marked KM) occurs from the southern side of the study area, trending
361 roughly NE–SW across the MTL. These anomalies agree with the results of Nishida et al. (2008),
362 which indicated comparable S-wave velocities in those areas, particularly at a depth of about 2 km
363 (see Figure 20 in Nishida et al., 2008). Between the two distinct high-velocity zones exhibited in
364 Nishida et al. (2008), an elongated low-velocity anomaly is evident. Likewise, a prominent low-
365 velocity anomaly is apparent in our results, flanked on both sides by high-velocity zones (NM and
366 KM) and trending roughly NE–SW. Although our results and those of Nishida et al. (2008) at a
367 depth of about 2 km are similar, our results show prevalent small-scale (~10 km) low-velocity
368 features at a depth of about 2 km and shallower. In the S-wave velocity model of Nishida et al.
369 (2008), such narrow low-velocity zones could not be revealed. The higher lateral resolution of our
370 velocity model at shallow depths (≤ 2 km) than Nishida et al. (2008) model ascribes to the use of
371 shorter wavelength surface waves and the dense seismic array. Most importantly, prominent
372 anomalies identified in our results correlate well with known geologic features, including fault
373 zones, sedimentary basins, and mountain ranges.



374

375 **Figure 7.** S-wave velocity models at different depths below sea level, given above each panel. (a–f) S-
 376 wave velocity models without showing the active faults (S-wave velocity models before topographic
 377 correction are shown in Figure S4). NM and KM represent the prominent high-velocity anomalies.

378



379

380 **Figure 8.** S-wave velocity models at different depths below sea level, given above each panel. (a–d) S-
 381 wave velocity models overlaid with active faults (black lines). Also shown is the location of the Median
 382 Tectonic Line (MTL).
 383

383

384 5 Interpretations

385 We attribute the high S-wave velocity anomaly observed in the northwestern part of the study area
 386 (marked NM in Figures 7f and 9b) to the presence of the Yakuno intrusive rocks and the
 387 Mino/Tamba belts (Figure 1a). The Yakuno intrusive rocks constitute the Maizuru zone, and the
 388 Mino/Tamba belts are Jurassic accretionary complexes composed of non-marine sediments, and
 389 the extensively distributed granite batholith (Matsushita, 1963; Nakae, 1993; Nakajima, 1994).

390 Towards the edges of the study area, the resolution of our S-wave velocity model is compromised
391 by the moderate-low ray paths coverage. However, an extensive low-velocity anomaly proximal
392 to the Sea of Japan (NLV in Figure 7a) is evident. This low-velocity anomaly is attributable to the
393 presence of the Tango-Tajima terrain, which is composed of the Neogene volcanic and
394 sedimentary series (Matsushita, 1963). The high velocities on the southeastern side of the study
395 area (around the MTL) may be indicating the presence of the zonally arranged Sanbagawa
396 metamorphic terrain, which consists of the dynamo-thermally metamorphosed Paleozoic, the
397 Chichibu terrain, which is composed chiefly of Paleozoic and fossiliferous Mesozoic, and the
398 Hidaka terrain with undivided Mesozoic and scanty fossils (Figure 1a).

399 A prominent elongated NE–SW trending low-velocity anomaly occurring at the boundary between
400 the high-velocity anomalies denoted by NM and KM (Figures 7f and 9b) is observed. This low-
401 velocity anomaly coincides with the Niigata–Kobe Tectonic Zone (NKTZ, Figure 1a) and the
402 Biwako-seigan Fault Zone on the western shoreline of Lake Biwa (BSFZ; Figures 9b and 11a).
403 The BSFZ is constituted of the NNE–SSW-trending west-dipping faults separated by clear small
404 gaps or steps (e.g., the Chinai, Aibano, Kamidera, Katsuno, Hira, Katata, Hiei, and Zeze faults;
405 Figure 11a), and is reported to have a reverse fault sense of east side subsidence (Takemura et al.,
406 2013). The location of some members of the BSFZ clearly coincide with the boundary between
407 the low-velocity zone (Lake Biwa) and the high-velocity zone in our topography-corrected S-wave
408 velocity models (Hira-Hiei mountains; Figure 11). On the western side of Mt. Hira, the observed
409 NNE-SSW trending linear low-velocity anomaly is consistent with the location of the Hanaore
410 Fault (HOF; Figure 11a), which is a ~50-km-long, right-lateral strike-slip Fault (Noda &
411 Shimamoto, 2009). However, the effects of BSFZ and HOF are not clearly visible in S-wave
412 velocity models without topography correction (Figure S7).

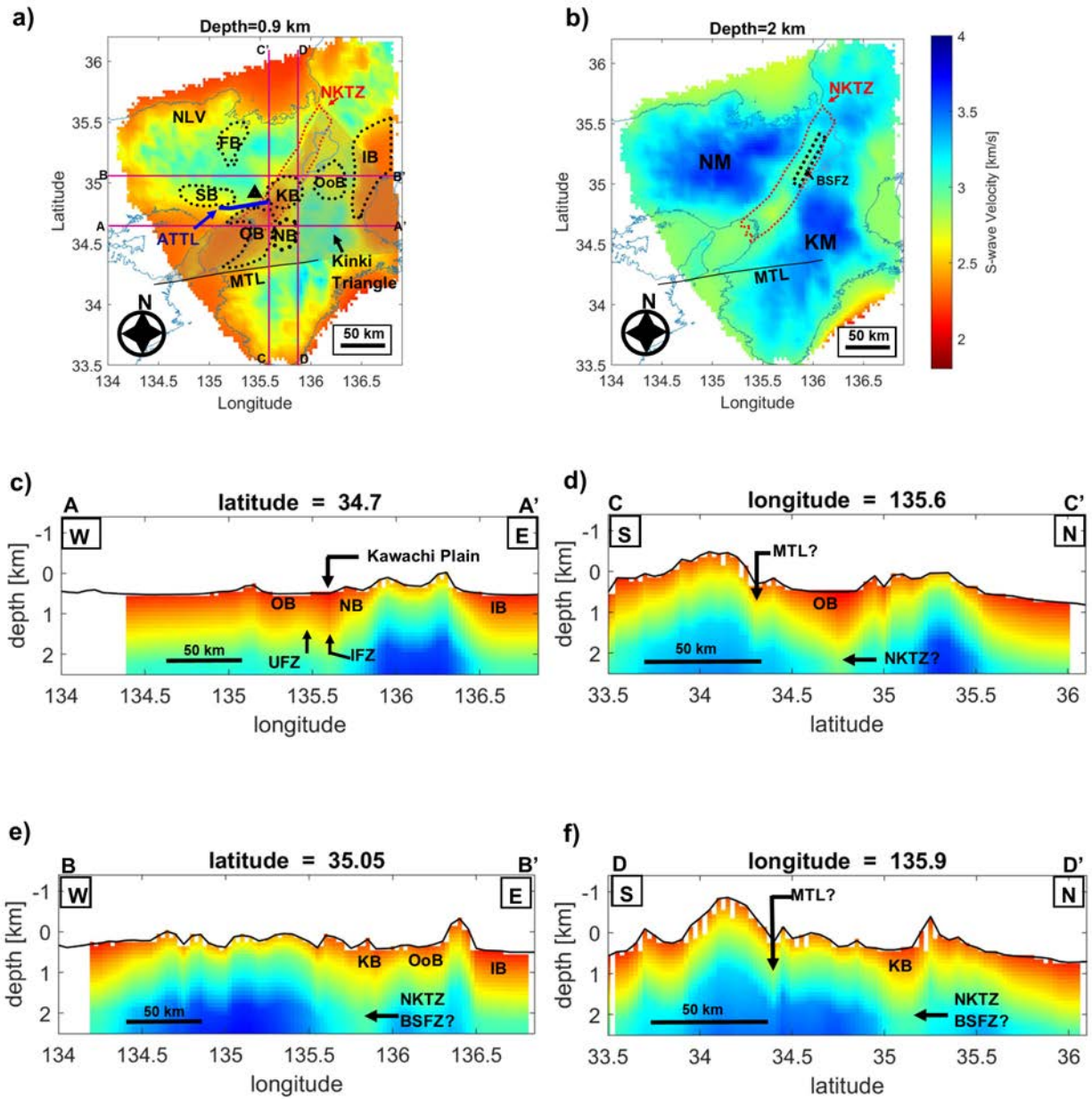
413 Both the western and eastern sides of the NKTZ are characterized by conspicuous fault systems,
414 with some major faults running through geological units, such as the Yagi-Yabu faults (YGF-
415 YBF) and the Mitoke Fault (MTF) (Mogi et al., 1991). The intervening spaces between fault pairs
416 such as the YGF–YBF and MTF faults are often located in the terrace and the alluvial plain
417 (Katsura, 1990). In our results, the low-velocity anomaly observed between the YGF–YBF and
418 the MTF (Figure 11) probably represent sedimentary units within and around the Fukuchiyama
419 basin (FB), but may also be indicating a possibility of the existence of active faults interconnecting
420 these fault pairs. Besides the gaps between pairs of known active faults, several narrow, elongated
421 low-velocity anomalies are identified, which, to some extent, coincide well with the locations of
422 known active faults. Nonetheless, there are cases where the observed elongated low-velocity
423 anomalies and the locations of known active faults do not correspond (Figures 10-11). Such
424 elongated low-velocity anomalies are largely trending to the NW–SE and NE–SW directions. We
425 posit that some of these linear low-velocity zones are likely to be attributable to the weathering
426 effects and sediments associated with the activity of undocumented concealed faults or fault zones.
427 On the southern side of the Kinki region, alternating linear low- and high-velocity zones are
428 pronounced (demarcated by a blue curly bracket in Figure 10b), attributable to the presence of
429 sediments within meridional deep valleys and mountain ranges, respectively (Matsushita, 1963).

430 Distinct low-velocity anomalies occur at the Sanda basin (SB), FB, Osaka basin (OB), Nara basin
431 (NB), Kyoto basin (KB), Oomi basin (OoB), and the Ise basin (IB) (Figure 9). The OB manifest
432 as a near-elliptical low-velocity zone, with the northern and southern edges of this zone appearing
433 to be oriented ENE–WSW and NE–SW, respectively. The low-velocity values in this area are

434 likely to be representing the Plio-Pleistocene Osaka Group sediments, which are discordantly
435 overlain by terrace and alluvial deposits (Itihara et al., 1997). The ENE–WSW trending northern
436 boundary of the OB coincides with the location of the Arima-Takatsuki Tectonic Line (ATTL;
437 blue line in Figure 9a). The ATTL is reported to be striking in an ENE–WSW direction, nearly
438 parallel to the MTL (Mitchell et al., 2011), and is characterized by a linear fault zone and steep
439 fault surfaces. Based on this notion, the ATTL marks the boundary between high-velocity zones
440 (mountainous regions; e.g., the Hokusetsu Mountains) and low-velocity zones (basins; e.g., the SB
441 and OB in Figure 9a).

442 According to Hallo et al. (2019), the OB is bounded by two near-parallel reverse faults on its
443 eastern margin, the Uemachi Fault Zone (UFZ) and the Ikoma Fault Zone (IFZ). However, the
444 effect of these fault zones is not clear in our results. Even so, our results show a low-velocity
445 anomaly stretching to deeper parts of the displayed vertical sections (Figure 9c) occurring between
446 known locations of the UFZ and IFZ. This low-velocity anomaly corresponds to a sub-basin of the
447 OB between the elevated areas of Ikoma and Uemachi Upland (Figure 9c), designated the Kawachi
448 plain (Hatayama et al., 1995). The high-velocity basement material exhibits undulating
449 topographic pattern, with some synclinal parts representing depressional areas in which deep
450 sedimentary basins occur and anticlinal parts corresponding to the basement upheavals or
451 mountain ranges (Figures 9c-f and 10c-d). Since surface wave inversion is strongly sensitive to
452 the presence of sediments, the low-velocity anomalies observed at depressional areas are
453 postulated to be representing the prevailing thick sediments (Miyamura et al., 1981; Nakayama,
454 1996; Takemura, 1985). At the Ise basin (IB, Figure 9e), the high-velocity material appears to have
455 subsided significantly. This subsidence may be reflecting the effects of the Kuwana and the
456 Yokkaichi reverse faults, which form part of the nearly N–S trending Yoro fault system (Research
457 Group for Active Faults of Japan, 1991). Similar discontinuities within the high-velocity material
458 are evident beneath the OB and KB low-velocity material (Figure 9c-f), likely to be representing
459 the effects of the NKTZ and/or BSFZ.

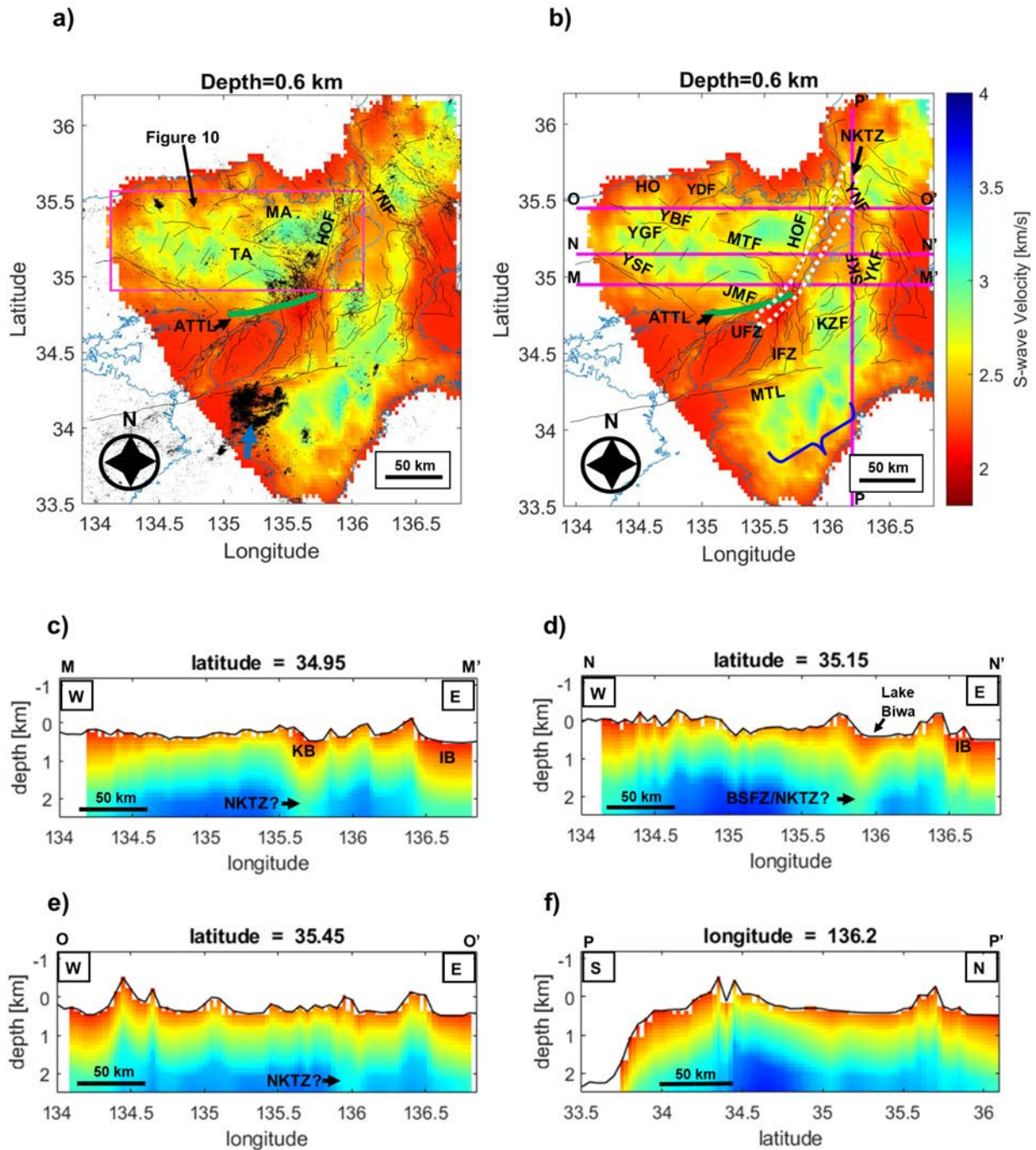
460



461
 462 **Figure 9.** S-wave velocity structure at 0.9 km (a) and 2 km (b) depths below sea level, and vertical slices
 463 (c–f) through the S-wave velocity structure along the profiles marked in a, showing the variation of S-
 464 wave velocity with depth (bottom panels) and their respective elevation models in km (top panels). The
 465 solid black line represents the Median Tectonic Line (MTL), the dashed red closed-curve represents the
 466 Niigata-Kobe Tectonic Zone (NKTZ), and the thick solid blue line indicates the location of the Arima-
 467 Takatsuki Tectonic Line (ATTL). The gray-shaded area represents the Kinki triangle. Black triangle
 468 represents the location of Hokusetsu mountains. Thin, dashed black closed-curves show the locations of
 469 major sedimentary basins (SB, Sanda basin; FB, Fukuchiyama basin; OB, Osaka basin; NB, Nara basin;
 470 OoB, Oomi basin; KB, Kyoto basin; and IB, Ise basin). Also shown on the depth slices are the probable
 471 locations of the Kawachi plain, Nara basin (NB), Uemachi Fault Zone (UFZ), Ikoma Fault Zone (IFZ),
 472 Biwako-seigan Fault Zone (BSFZ), NKTZ, Osaka basin (OB), and Ise basin (IB).
 473

474 To assess the seismic activity correlating to the distribution of anomalous zones identified in this
475 study, we superimposed earthquake hypocenters for the period 2001–2012 (Yano et al., 2017) on
476 the S-wave velocity model (Figures 10a, 11b). Numerous earthquake hypocenters are distributed
477 across the high-velocity zone on the western side of Hira mountain (Mt. Hira in Figure 11b). By
478 contrast, hypocenter clusters are evident on the low-velocity zone occurring between the eastern
479 margin of the TA and MA tectonic blocks, western part of the HOF and the northern side of ATTL
480 (Figures 10 and 11). Besides these notable clusters, the northwestern part of the Kinki region has
481 a wide distribution of hypocenters, some of which are aligned in the same trend as elongated low-
482 velocity zones or along the contact between low- and high-velocity zones (Figures 10a and 11b).
483 Some of the linear low-velocity zones which are not consistent with the location of known active
484 faults but exhibiting chains of earthquake hypocenters (Figure 11b) may be representing the
485 weathering effects and sediments associated with the activity of undocumented concealed faults
486 or fault zones.

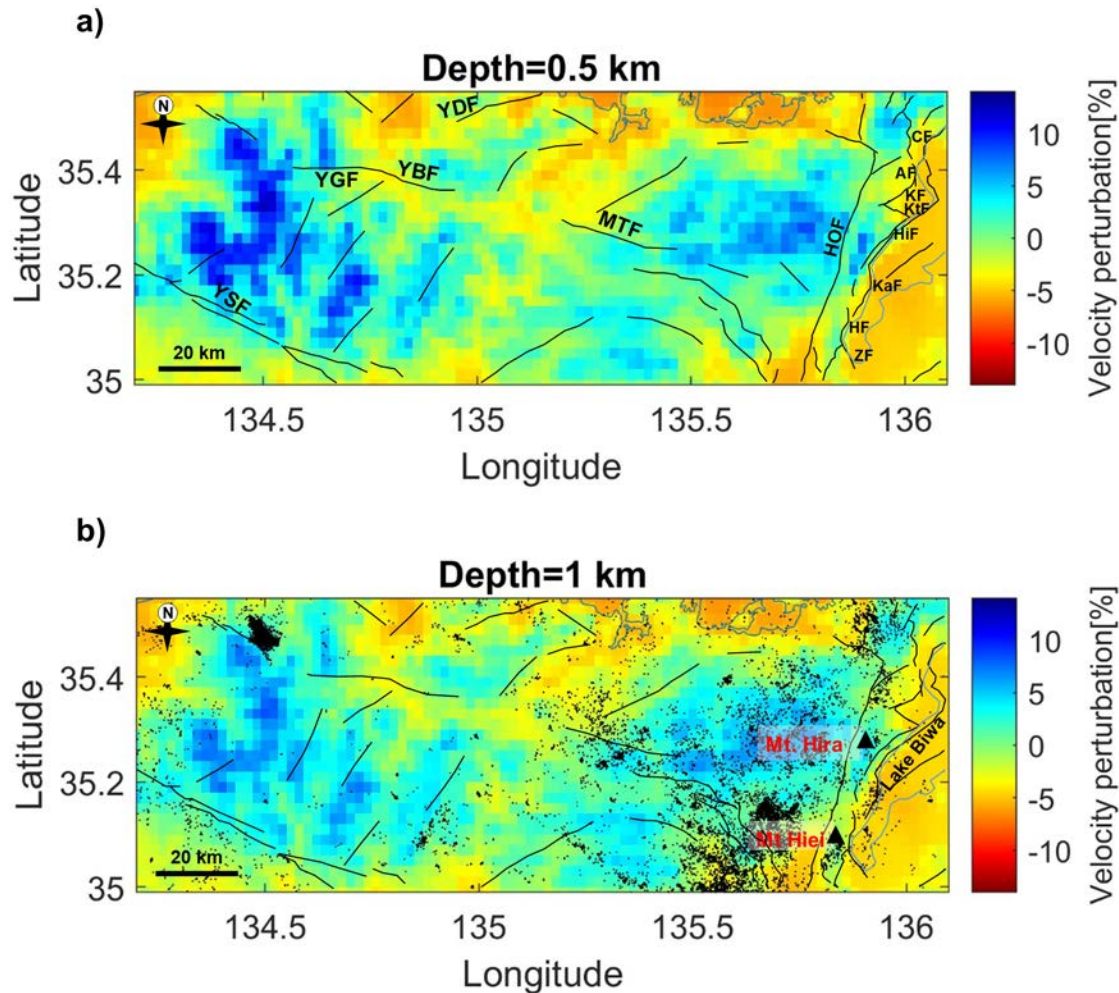
487 A dense distribution of earthquake hypocenters is observed in the low-velocity zone along the
488 western part of the Kii Mountainland (blue arrow in Figure 10a). These conspicuous seismic events
489 appear to terminate to the north at the near ENE-WSW trending low-velocity zone, consistent with
490 the location of the MTL. According to Kanamori and Tsumura (1971), increased seismicity to the
491 south of the MTL is related to the regional structural heterogeneities associated with the past
492 activity of the MTL, rather than to the local geological structures.
493



494
495
496
497
498
499
500
501
502
503
504

Figure 10. (a) Map of seismic events that occurred between January 2001 and December 2012 (Yano et al., 2017) superimposed on the S-wave velocity model horizontal slice at 0.6 km depth below sea level. Plotted hypocenters (black dots) are for earthquakes ranging from 0 to 6.5 in moment magnitude for depths shallower than 12 km. Blue arrow indicates the location of dense distribution of earthquake hypocenters along the western part of the Kii Mountainland. (b) Distribution of active faults superimposed on the S-wave velocity model horizontal slice at 0.6 km depth below sea level. Solid black lines represent active faults documented prior to this study (Research Group for Active Faults of Japan, 1991). Thick dashed white closed-curve and a solid green line indicate the locations of the Niigata–Kobe Tectonic Zone (NKTZ) and the Arima–Takatsuki Tectonic Line (ATTL), respectively. Also shown are the locations of the Median Tectonic Line (MTL), Yamada Fault (YDF), Yamasaki Fault (YSF),

505 Jumantsuji Fault (JMF, a member of the ATTL), Yabu Fault (YBF), Yagi Fault (YGF), Mitoke Fault
 506 (MTF), Hanaori Fault (HOF), Kizugawa Fault (KZF), Suzuka Fault (SKF), Yokkaichi Fault (YKF),
 507 Yanagase Fault (YNF), Uemachi Fault Zone (UFZ), Ikoma Fault Zone (IFZ), Tanba Block (TA), Hokutan
 508 Block (HO), and the Maizuru Block (MA). Blue curly bracket marks the location of three alternating
 509 meridional deep valleys and mountain ranges. (c–f) Vertical sections of S-wave velocity along the
 510 profiles marked as solid magenta lines in Figure 9b. Inferred locations of the Kyoto basin (KB), Ise basin
 511 (IB), Lake Biwa and the Biwako-seigan Fault Zone (BSFZ) and/or Niigata-Kobe Tectonic Line (NKTZ)
 512 along the profile are also shown on the vertical sections.
 513



514

515 **Figure 11.** Enlarged view of the northern part of the Kinki region (shown in Figure 9). (a) S-wave
 516 velocity perturbation at a depth of 0.5 km below sea level. Also shown are the locations of the Yamada
 517 Fault (YDF), Yamasaki Fault (YSF), Yagi-Yabu Fault (YGF-YBF), Mitoke Fault (MTF), Hanaore Fault
 518 (HOF) and the Biwako-seigan Fault Zone members (Chinai Fault, CF; Aibano Fault, AF; Kamidera Fault,
 519 KF; Katsuno, KtF; Hira Fault, HiF; Katata, KaF; Hiei Fault, HF; Zeze Fault, ZF) (Kaneda et al., 2008).
 520 (b) S-wave velocity perturbation at a depth of 1 km below sea level, overlaid with earthquake hypocenters
 521 (black dots; Yano et al., 2017) and active faults. Black triangles represent the Hira and Hiei mountains.
 522 Solid black lines represent documented active faults (Research Group for Active Faults of Japan, 1991).
 523

524 **6 Conclusions**

525 We constructed a high-resolution shallow 3D S-wave velocity structure of the Kinki region using
526 data recorded by the 221 temporary and permanent seismic stations. We used the zero-crossing
527 method to estimate S-wave phase velocity measurements in the frequency domain. We then
528 applied a direct surface wave tomographic inversion method using high-frequency ambient noise
529 data (0.083–0.67 Hz and 0.05–0.95 Hz). Our results revealed that S-wave velocities vary
530 significantly in the vertical and horizontal directions, which is consistent with the heterogeneous
531 geology of the Kinki region. Conspicuous high-velocity zones are identified in the northwestern
532 and southeastern parts of the study area and are attributed to shallow basement material,
533 mountainous regions, or sedimentary complexes. Sedimentary basins manifest as low-velocity
534 zones. Using horizontal and depth slices of the S-wave velocity model, we estimated the locations
535 of the recently reactivated Niigata-Kobe Tectonic Zone and the highly active Arima-Takatsuki
536 Tectonic Line on the northern edge of the Osaka basin. In the western coast area of Lake Biwa,
537 effects of the active Biwako-seigan Fault Zone are revealed clearly in our results (Figure 8e–f).

538 We also identified several fine-scale low-velocity tectonic structures, coexisting with known active
539 faults, such as the N–S-, ENE–WSW-, and NE–SW-trending active faults on the eastern side of
540 the Niigata–Kobe Tectonic Zone. In addition, our results revealed elongated low-velocity features
541 that are not consistent with known active faults, likely to be indicating a possible existence of
542 unidentified faults (largely NW–SE- and NE–SW-trending faults) across the Kinki region. These
543 findings allude to the improved resolution of our S-wave velocity model compared with previous
544 studies of the Kinki region. The observed probable concealed fault zones (linear low-velocity
545 anomalies) characterized by aligned distribution of earthquake hypocenters will be useful for
546 hazard assessment and disaster mitigation. The alternating pattern of subsided and uplifted zones
547 observed in vertical slices of our S-wave velocity model is consistent with the tectonic history of
548 the Kinki triangle, which has been dominated by the E–W compressional movement and is also an
549 area characterized by a dense distribution of active faults. These results improve our understanding
550 of shallow crustal structure in the Kinki region. Furthermore, a good correlation between
551 heterogeneities in the S-wave velocity model and the spatial distribution of fault traces and other
552 geologic features in the Kinki region suggests that the approach adopted in this study can be
553 utilized as an effective method for unraveling the complex crustal structure of environments akin
554 to the Kinki region.

555 **Acknowledgments**

556 Seismic data were obtained from the National Research Institute for Earth Science and Disaster
557 Resilience, the National Institute of Advanced Industrial Science and Technology, the Japan
558 Meteorological Agency, the Disaster Prevention Research Institute of Kyoto University,
559 University of Tokyo, Nagoya University, and Kyushu University. We used earthquake
560 hypocenters made available by the Japan Unified hi-resolution relocated Catalog for Earthquakes
561 (JUICE) project. The computations in this work were partly performed using the computer
562 facilities at the Research Institute for Information Technology, Kyushu University. This work was
563 supported by JSPS KAKENHI (Grant Numbers JP19K23544, JP20K04133, and JP20H01997).

564 **References**

- 565 Aki, K. (1957). Space and time spectra of stationary stochastic waves, with special reference to
 566 microtremors. *Bulletin of the Earthquake Research Institute*, 35(3), 415-456.
- 567 Anon (n.d.). Geological survey of Japan, AIST. Available from:
 568 <https://gbank.gsj.jp/subsurface/english/ondemand.php> (Accessed 19 November 2021)
- 569 Aoki, S., Iio, Y., Katao, H., Miura, T., Yoneda, I., & Sawada, M. (2016). Three-dimensional
 570 distribution of S wave reflectors in the northern Kinki district, southwestern Japan. *Earth,*
 571 *Planets and Space*, 68(1), 1-9. <https://doi.org/10.1186/s40623-016-0468-3>
- 572 Asano, K., Iwata, T., Sekiguchi, H., Somei, K., Miyakoshi, K., Aoi, S., & Kunugi, T. (2017).
 573 Surface wave group velocity in the Osaka sedimentary basin, Japan, estimated using ambient
 574 noise cross-correlation functions. *Earth, Planets and Space*, 69(1), 1-20.
 575 <https://doi.org/10.1186/s40623-017-0694-3>
- 576 Asten, M. W. (2006). On bias and noise in passive seismic data from finite circular array data
 577 processed using SPAC methods. *Geophysics*, 71(6), V153-V162.
 578 <https://doi.org/10.1190/1.2345054>
- 579 Barnes, G. L. (2008). The making of the Japan Sea and the Japanese Mountains: understanding
 580 Japan's volcanism in structural context. *Nichibunken Japan Review*, 20, 3-52.
- 581 Bensen, G. D., Ritzwoller, M. H., Barmin, M. P., Levshin, A. L., Lin, F., Moschetti, M. P., et al.
 582 (2007). Processing seismic ambient noise data to obtain reliable broad-band surface wave
 583 dispersion measurements. *Geophysical Journal International*, 169(3), 1239-1260.
 584 <https://doi.org/10.1111/j.1365-246X.2007.03374.x>
- 585 Boschi, L., & Ekström, G. (2002). New images of the Earth's upper mantle from measurements of
 586 surface wave phase velocity anomalies. *Journal of Geophysical Research: Solid*
 587 *Earth*, 107(B4), ESE-1. <https://doi.org/10.1029/2000JB000059>
- 588 Brown, M. (2010). Paired metamorphic belts revisited. *Gondwana Research*, 18(1), 46-59.
 589 <https://doi.org/10.1016/j.gr.2009.11.004>
- 590 Chen, K. X., Gung, Y., Kuo, B. Y., & Huang, T. Y. (2018). Crustal magmatism and deformation
 591 fabrics in northeast Japan revealed by ambient noise tomography. *Journal of Geophysical*
 592 *Research: Solid Earth*, 123(10), 8891-8906. <https://doi.org/10.1029/2017JB015209>
- 593 Cho, I., Senna, S., Wakai, A., Jin, K., & Fujiwara, H. (2021). Basic performance of a spatial
 594 autocorrelation method for determining phase velocities of Rayleigh waves from microtremors,
 595 with special reference to the zero-crossing method for quick surveys with mobile seismic
 596 arrays. *Geophysical Journal International*, 226(3), 1676-1694.
 597 <https://doi.org/10.1093/gji/ggab149>
- 598 Ekström, G., Abers, G. A., & Webb, S. C. (2009). Determination of surface-wave phase velocities
 599 across USArray from noise and Aki's spectral formulation. *Geophysical Research*
 600 *Letters*, 36(18). <https://doi.org/10.1029/2009GL039131>
- 601 Ekström, G. (2014). Love and Rayleigh phase-velocity maps, 5–40 s, of the western and central
 602 USA from USArray data. *Earth and Planetary Science Letters*, 402, 42-49.
 603 <https://doi.org/10.1016/j.epsl.2013.11.022>
- 604 Fang, H., Yao, H., Zhang, H., Huang, Y. C., & van der Hilst, R. D. (2015). Direct inversion of
 605 surface wave dispersion for three-dimensional shallow crustal structure based on ray tracing:
 606 methodology and application. *Geophysical Journal International*, 201(3), 1251-1263.
 607 <https://doi.org/10.1093/gji/ggv080>

- 608 Feng, M., & An, M. (2010). Lithospheric structure of the Chinese mainland determined from joint
609 inversion of regional and teleseismic Rayleigh-wave group velocities. *Journal of Geophysical*
610 *Research: Solid Earth*, 115(B6). <https://doi.org/10.1029/2008JB005787>
- 611 Foti, S., Lai, C. G., Rix, G. J., & Strobbia, C. (2014). *Surface wave methods for near-surface site*
612 *characterization*. CRC press, Taylor & Francis Group LLC.
- 613 Gu, N., Wang, K., Gao, J., Ding, N., Yao, H., & Zhang, H. (2019). Shallow crustal structure of the
614 Tanlu Fault Zone near Chao Lake in eastern China by direct surface wave tomography from
615 local dense array ambient noise analysis. *Pure and Applied Geophysics*, 176(3), 1193-1206.
616 <https://doi.org/10.1007/s00024-018-2041-4>
- 617 Hallo, M., Opršal, I., Asano, K., & Gallovič, F. (2019). Seismotectonics of the 2018 northern
618 Osaka M6. 1 earthquake and its aftershocks: joint movements on strike-slip and reverse faults
619 in inland Japan. *Earth, Planets and Space*, 71(1), 1-21. [https://doi.org/10.1186/s40623-019-](https://doi.org/10.1186/s40623-019-1016-8)
620 1016-8
- 621 Hatayama, K., Matsunami, K., Iwata, T., & Irikura, K. (1995). Basin-induced Love waves in the
622 eastern part of the Osaka basin. *Journal of Physics of the Earth*, 43(2), 131-155.
623 <https://doi.org/10.4294/jpe1952.43.131>
- 624 Hayashi, K. (2008). Development of surface-wave methods and its application to site
625 investigations, (Doctoral dissertation). Retrieved from Kyoto University Research
626 Information Repository. (<http://hdl.handle.net/2433/57255>). Japan: Kyoto University.
- 627 Huzita, K. (1969). Tectonic development of southwest Japan in the Quaternary period. *Journal of*
628 *Geosciences Osaka City University*, 12(5), 53-73.
- 629 Huzita, K. (1980). Role of the Median Tectonic Line in the Quaternary tectonics of the Japanese
630 Islands. *Mem. Geol. Soc. Jpn.*, 18, 129-153.
- 631 Huzita, K., Kishimoto, Y., & Shiono, K. (1973). Neotectonics and seismicity in the Kinki area,
632 Southwest Japan. *Journal of Geosciences Osaka City University*, 16(6), 93-124.
- 633 Hyodo, M., & Hirahara, K. (2003). A viscoelastic model of interseismic strain concentration in
634 Niigata-Kobe Tectonic Zone of central Japan. *Earth, planets and space*, 55(11), 667-675.
635 <https://doi.org/10.1186/BF03352473>
- 636 Iio, Y. (1996). A possible generating process of the 1995 southern Hyogo Prefecture earthquake:
637 Stick of fault and slip on detachment. *Jishin*, 49(1), 103-112.
638 https://doi.org/10.4294/zisin1948.49.1_103
- 639 Iio, Y., Kishimoto, S., Nakao, S., Miura, T., Yoneda, I., Sawada, M., & Katao, H. (2018).
640 Extremely weak fault planes: an estimate of focal mechanisms from stationary seismic activity
641 in the San'in district, Japan. *Tectonophysics*, 723, 136-148.
642 <https://doi.org/10.1016/j.tecto.2017.12.007>
- 643 Itihara, M., Yoshikawa, S., & Kamei, T. (1997). 24 The Pliocene-Pleistocene boundary in Japan:
644 the Osaka Group. *The Pleistocene Boundary and the Beginning of the Quaternary*, 41, 239.
645 <https://doi.org/10.1017/CBO9780511585760.026>
- 646 Ito, K., Umeda, Y., Sato, H., Hirose, I., Hirata, N., Kawanaka, T., & Ikawa, T. (2006). Deep
647 seismic surveys in the Kinki district: Shingu-Maizuru line. *Bull. Earthquake Res. Inst. Univ.*
648 *Tokyo*, 81, 239-245.
- 649 Kanamori, H. (1995). The Kobe (Hyogo-ken Nanbu), Japan, earthquake of January 16,
650 1995. *Seismological Research Letters*, 66(2), 6-10. <https://doi.org/10.1785/gssrl.66.2.6>
- 651 Kanamori, H., & Tsumura, K. (1971). Spatial distribution of earthquakes in the Kii peninsula,
652 Japan, south of the Median Tectonic Line. *Tectonophysics*, 12(4), 327-342.
653 [https://doi.org/10.1016/0040-1951\(71\)90020-5](https://doi.org/10.1016/0040-1951(71)90020-5)

- 654 Kaneda, H., Kinoshita, H., & Komatsubara, T. (2008). An 18,000-year record of recurrent folding
655 inferred from sediment slices and cores across a blind segment of the Biwako-seigan fault
656 zone, central Japan. *Journal of Geophysical Research: Solid Earth*, 113(B5).
657 <https://doi.org/10.1029/2007JB005300>
- 658 Katao, H., Maeda, N., Hiramatsu, Y., Iio, Y., & Nakao, S. (1997). Detailed mapping of focal
659 mechanisms in/around the 1995 Hyogo-ken Nanbu earthquake rupture zone. *Journal of*
660 *Physics of the Earth*, 45(2), 105-119. <https://doi.org/10.4294/jpe1952.45.105>
- 661 Kato, A., & Ueda, T. (2019). Source fault model of the 2018 M w 5.6 northern Osaka earthquake,
662 Japan, inferred from the aftershock sequence. *Earth, Planets and Space*, 71(1), 1-9.
663 <https://doi.org/10.1186/s40623-019-0995-9>
- 664 Katoh, S., Iio, Y., Katao, H., Sawada, M., Tomisaka, K., Miura, T., & Yoneda, I. (2018). The
665 relationship between S-wave reflectors and deep low-frequency earthquakes in the northern
666 Kinki district, southwestern Japan. *Earth, Planets and Space*, 70(1), 1-11.
667 <https://doi.org/10.1186/s40623-018-0921-6>
- 668 Katsura, I. (1990). Block structure bounded by active strike-slip faults in the northern part of Kinki
669 district, southwest Japan. *Memoirs of the Faculty of Science, Kyoto University. Series of*
670 *geology and mineralogy*, 55(1-2), 57-123. Retrieved from Kyoto University Research
671 Information Repository. (<http://hdl.handle.net/2433/186665>)
- 672 Lin, F. C., Li, D., Clayton, R. W., & Hollis, D. (2013). High-resolution 3D shallow crustal structure
673 in Long Beach, California: Application of ambient noise tomography on a dense seismic
674 array. *Geophysics*, 78(4), Q45-Q56. <https://doi.org/10.1190/geo2012-0453.1>
- 675 Lin, F. C., Moschetti, M. P., & Ritzwoller, M. H. (2008). Surface wave tomography of the western
676 United States from ambient seismic noise: Rayleigh and Love wave phase velocity
677 maps. *Geophysical Journal International*, 173(1), 281-298. [https://doi.org/10.1111/j.1365-](https://doi.org/10.1111/j.1365-246X.2008.03720.x)
678 [246X.2008.03720.x](https://doi.org/10.1111/j.1365-246X.2008.03720.x)
- 679 Matsubara, M., Obara, K., & Kasahara, K. (2008). Three-dimensional P-and S-wave velocity
680 structures beneath the Japan Islands obtained by high-density seismic stations by seismic
681 tomography. *Tectonophysics*, 454(1-4), 86-103. <https://doi.org/10.1016/j.tecto.2008.04.016>
- 682 Matsushita, S. (1963). Geological history of the Kinki District, Japan during the Cainozoic Era
683 (Preliminary note). *Special Contributions of the Geophysical Institute, Kyoto University*, 2,
684 113-124. Retrieved from Kyoto University Research Information Repository.
685 (<http://hdl.handle.net/2433/178442>)
- 686 Matsushita, R., & Imanishi, K. (2015). Stress fields in and around metropolitan Osaka, Japan,
687 deduced from microearthquake focal mechanisms. *Tectonophysics*, 642, 46-57.
688 <https://doi.org/10.1016/j.tecto.2014.12.011>
- 689 Mitamura, M., Matsuyama, N., Nakagawa, K.,
690 Yamamoto, K., & Suwa, S. (1994). Stratigraphy and subsurface structure of Holocene deposits
691 around Uemachi Upland in the central Osaka Plain. *Journal of Geosciences, Osaka City*
University, 37, 183-212.
- 692 Mitchell, T. M., Ben-Zion, Y., & Shimamoto, T. (2011). Pulverized fault rocks and damage
693 asymmetry along the Arima-Takatsuki Tectonic Line, Japan. *Earth and Planetary Science*
694 *Letters*, 308(3-4), 284-297. <https://doi.org/10.1016/j.epsl.2011.04.023>
- 695 Miyamura, M., Yoshida, F., Yamada, N., Sato, T., & Sangawa, A. (1981). Geology of the
696 Kameyama district: Quadrangle Series. *Geological Survey of Japan*, 128.
- 697 Mogi, T., Katsura, I., & Nishimura, S. (1991). Magnetotelluric survey of an active fault system in
698 the northern part of Kinki District, southwest Japan. *Journal of structural geology*, 13(2), 235-
699 240. [https://doi.org/10.1016/0191-8141\(91\)90070-Y](https://doi.org/10.1016/0191-8141(91)90070-Y)

- 700 Nakae, S. (1993). Jurassic accretionary complex of the Tamba Terrane, Southwest Japan, and its
701 formative process. *Journal of Geosciences, Osaka City University*, 36, 15-70.
- 702 Nakajima, T. (1994). The Ryoke plutonometamorphic belt: crustal section of the Cretaceous
703 Eurasian continental margin. *Lithos*, 33(1-3), 51-66. [https://doi.org/10.1016/0024-4937\(94\)90053-1](https://doi.org/10.1016/0024-4937(94)90053-1)
- 704
705 Nakajima, J., Hirose, F., & Hasegawa, A. (2009). Seismotectonics beneath the Tokyo metropolitan
706 area, Japan: Effect of slab-slab contact and overlap on seismicity. *Journal of Geophysical
707 Research: Solid Earth*, 114(B8). <https://doi.org/10.1029/2008JB006101>
- 708 Nakayama, K. (1996). Depositional models for fluvial sediments in an intra-arc basin: an example
709 from the Upper Cenozoic Tokai Group in Japan. *Sedimentary Geology*, 101(3-4), 193-211.
710 [https://doi.org/10.1016/0037-0738\(95\)00065-8](https://doi.org/10.1016/0037-0738(95)00065-8)
- 711 Nimiya, H., Ikeda, T., & Tsuji, T. (2020). Three-Dimensional S Wave Velocity Structure of
712 Central Japan Estimated by Surface-Wave Tomography Using Ambient Noise. *Journal of
713 Geophysical Research: Solid Earth*, 125(4), e2019JB019043.
714 <https://doi.org/10.1029/2019JB019043>
- 715 Nishida, K., Kawakatsu, H., & Obara, K. (2008). Three-dimensional crustal S wave velocity
716 structure in Japan using microseismic data recorded by Hi-net tiltmeters. *Journal of
717 Geophysical Research: Solid Earth*, 113(B10). <https://doi.org/10.1029/2007JB005395>
- 718 Nishiwaki, H., Okudaira, T., Ishii, K., & Mitamura, M. (2021). Dip angles of active faults from
719 the surface to the seismogenic zone inferred from a 2D numerical analysis of visco-elasto-
720 plastic models: a case study for the Osaka Plain. *Earth, Planets and Space*, 73(1), 1-18.
721 <https://doi.org/10.1186/s40623-021-01390-8>
- 722 Noda, H., & Shimamoto, T. (2009). Constitutive properties of clayey fault gouge from the Hanaore
723 fault zone, southwest Japan. *Journal of Geophysical Research: Solid Earth*, 114(B4).
724 <https://doi.org/10.1029/2008JB005683>
- 725 Obara, K., Kasahara, K., Hori, S., & Okada, Y. (2005). A densely distributed high-sensitivity
726 seismograph network in Japan: Hi-net by National Research Institute for Earth Science and
727 Disaster Prevention. *Review of scientific instruments*, 76(2), 021301.
728 <https://doi.org/10.1063/1.1854197>
- 729 Oike, K. (1976). Spatial and temporal distribution of micro-earthquakes and active faults. *Mem.
730 Geol. Soc. Japan*, 12, 59-73.
- 731 Pilz, M., Parolai, S., Picozzi, M., & Bindi, D. (2012). Three-dimensional shear wave velocity
732 imaging by ambient seismic noise tomography. *Geophysical Journal International*, 189(1),
733 501-512. <https://doi.org/10.1111/j.1365-246X.2011.05340.x>
- 734 Prieto, G. A., Lawrence, J. F., & Beroza, G. C. (2009). Anelastic Earth structure from the
735 coherency of the ambient seismic field. *Journal of Geophysical Research: Solid
736 Earth*, 114(B7). <https://doi.org/10.1029/2008JB006067>
- 737 Rawlinson, N., & Sambridge, M. (2004). Wave front evolution in strongly heterogeneous layered
738 media using the fast marching method. *Geophysical Journal International*, 156(3), 631-647.
739 <https://doi.org/10.1111/j.1365-246X.2004.02153.x>
- 740 Research Group for Active Faults of Japan. (1991). Active faults in Japan: Sheet maps and
741 inventories. University of Tokyo press, 437.
- 742 Sabra, K. G., Gerstoft, P., Roux, P., Kuperman, W. A., & Fehler, M. C. (2005). Surface wave
743 tomography from microseisms in Southern California. *Geophysical Research Letters*, 32(14).
744 <https://doi.org/10.1029/2005gl023155>

- 745 Sadeghisorkhani, H., Gudmundsson, Ó., & Tryggvason, A. (2018). GSpecDisp: A matlab GUI
746 package for phase-velocity dispersion measurements from ambient-noise
747 correlations. *Computers & Geosciences*, *110*, 41-53.
748 <https://doi.org/10.1016/j.cageo.2017.09.006>
- 749 Sagiya, T., Miyazaki, S. I., & Tada, T. (2000). Continuous GPS array and present-day crustal
750 deformation of Japan. *Pure and applied Geophysics*, *157*(11), 2303-2322.
751 <https://doi.org/10.1007/PL00022507>
- 752 Sato, H., Ito, K., Abe, S., Kato, N., Iwasaki, T., Hirata, N., et al. (2009). Deep seismic reflection
753 profiling across active reverse faults in the Kinki Triangle, central
754 Japan. *Tectonophysics*, *472*(1-4), 86-94. <https://doi.org/10.1016/j.tecto.2008.06.014>
- 755 Shapiro, N. M., Campillo, M., Stehly, L., & Ritzwoller, M. H. (2005). High-resolution surface-
756 wave tomography from ambient seismic noise. *Science*, *307*(5715), 1615-1618.
757 <https://doi.org/10.1126/science.1108339>
- 758 Shapiro, N. M., & Ritzwoller, M. H. (2002). Monte-Carlo inversion for a global shear-velocity
759 model of the crust and upper mantle. *Geophysical Journal International*, *151*(1), 88-105.
760 <https://doi.org/10.1046/j.1365-246X.2002.01742.x>
- 761 Suemoto, Y., Ikeda, T., Tsuji, T., & Iio, Y. (2020). Identification of a nascent tectonic boundary
762 in the San-in area, southwest Japan, using a 3D S-wave velocity structure obtained by ambient
763 noise surface wave tomography. *Earth, Planets and Space*, *72*(1), 1-13.
764 <https://doi.org/10.1186/s40623-020-1139-y>
- 765 Taira, A. (2001). Tectonic evolution of the Japanese island arc system. *Annual Review of Earth
766 and Planetary Sciences*, *29*(1), 109-134. <https://doi.org/10.1146/annurev.earth.29.1.109>
- 767 Takemura, K. (1985). The Plio-Pleistocene Tokai Group and the tectonic development around Ise
768 Bay of central Japan since Pliocene. *Memoirs of the Faculty of Science, Kyoto University.
769 Series of geology and mineralogy*, *51*(1-2), 21-96. Retrieved from Kyoto University Research
770 Information Repository. (<http://hdl.handle.net/2433/186655>)
- 771 Takemura, K., Haraguchi, T., Kusumoto, S., & Itoh, Y. (2013). Tectonic basin formation in and
772 around Lake Biwa, Central Japan. *Mechan. Sedim. Basin Form*, *9*, 209-229.
773 <https://doi.org/10.5772/56667>
- 774 Tsai, V. C., & Moschetti, M. P. (2010). An explicit relationship between time-domain noise
775 correlation and spatial autocorrelation (SPAC) results. *Geophysical Journal
776 International*, *182*(1), 454-460. <https://doi.org/10.1111/j.1365-246X.2010.04633.x>
- 777 Usami, T. (2003). Materials for comprehensive list of destructive earthquakes in Japan. Univ. of
778 Tokyo Press, Tokyo, 605.
- 779 Wakita, K. (2013). Geology and tectonics of Japanese islands: a review—the key to understanding
780 the geology of Asia. *Journal of Asian Earth Sciences*, *72*, 75-87.
781 <https://doi.org/10.1016/j.jseaes.2012.04.014>
- 782 Yang, Y. (2014). Application of teleseismic long-period surface waves from ambient noise in
783 regional surface wave tomography: a case study in western USA. *Geophysical Journal
784 International*, *198*(3), 1644-1652. <https://doi.org/10.1093/gji/ggu234>
- 785 Yano, T. E., Takeda, T., Matsubara, M., & Shiomi, K. (2017). Japan unified high-resolution
786 relocated catalog for earthquakes (JUICE): crustal seismicity beneath the Japanese
787 Islands. *Tectonophysics*, *702*, 19-28. <https://doi.org/10.1016/j.tecto.2017.02.017>
- 788 Yao, H., van Der Hilst, R. D., & De Hoop, M. V. (2006). Surface-wave array tomography in SE
789 Tibet from ambient seismic noise and two-station analysis—I. Phase velocity

- 790 maps. *Geophysical Journal International*, 166(2), 732-744. [https://doi.org/10.1111/j.1365-](https://doi.org/10.1111/j.1365-246X.2006.03028.x)
791 246X.2006.03028.x
- 792 Yao, H., Beghein, C., & Van Der Hilst, R. D. (2008). Surface wave array tomography in SE Tibet
793 from ambient seismic noise and two-station analysis-II. Crustal and upper-mantle
794 structure. *Geophysical Journal International*, 173(1), 205-219.
795 <https://doi.org/10.1111/j.1365-246X.2007.03696.x>
- 796 Yolsal-Cevikbilen, S., Biryol, C. B., Beck, S., Zandt, G., Taymaz, T., Adiyaman, H. E., & Özacar,
797 A. A. (2012). 3-D crustal structure along the North Anatolian Fault Zone in north-central
798 Anatolia revealed by local earthquake tomography. *Geophysical Journal International*, 188(3), 819-849. <https://doi.org/10.1111/j.1365-246X.2011.05313.x>
799